Available online at www.sciencedirect.com

ScienceDirect

Energy Procedia 43 (2013) 18 – 26

Energy Procedia

4th Workshop on Metallization for Crystalline Silicon Solar Cells

Surface recombination velocity measurements of metallized surfaces by photoluminescence imaging

Frode Kløw[a]*, Halvard Haug[a], Sean Erik Foss[a]

[a]Department of Solar Energy, Institute for Energy Technology (IFE), P.O. Box 40, NO-2027 Kjeller, Norway

Abstract

QSSPC-calibrated photoluminescence imaging (PLI) was used to determine the rear surface recombination velocity $S_{rear,eff}$ of p-type Si FZ wafers after processing of large area screen printed Al contacts with varying paste thickness and firing temperatures. The paste thickness was varied by changing the snap off in the screen printer, and the resulting back surface field (BSF) thickness was investigated by scanning electron microscopy. BSF thicknesses of between 1.4 and 6.2 µm were found. The BSF thickness saturated at high paste amounts combined with high firing temperatures while an increase in the eutectic layer thickness was observed. Several luminescence images were taken of each sample with different reference samples to assess the stability of the technique, and uncertainties are discussed.

Selection and peer-review under responsibility of Guy Beaucarne, Gunnar Schubert and Jaap Hoornstra

Keywords: Photoluminescence imaging; PLI; Aluminum back surface field; Al-BSF, surface recombination velocity; SRV.

1. Introduction

As solar cells are getting thinner and the bulk quality improves, the importance of surface recombination increases. The surface recombination velocity (SRV) of a metallized Si surface cannot be directly measured by the conventional quasi steady state photo conductance (QSSPC) method as the inductive photoconductance measurement is shielded by the metal. Camera based photoluminescence imaging (PLI) [1,2] is a technique which is better suited for this purpose, as the lifetime calibration can be done by an integrated QSSPC system on a non-metallized section of the sample.

Using QSSPC to calibrate a PLI image is possible when the optical properties of the QSSPC calibrated sample are similar to the sample or part of sample imaged with PLI. In the PLI setup a monochromatic laser creates electron-hole pairs that diffuse until they recombine. The radiative recombination produces photons that are collected by a Si CCD detector. However, the photoluminescence can also be reflected off the back surface of the sample, increasing the signal. Front surface reflection back into the sample will decrease the signal. Therefore, PLI will only give relative values for metallized samples, but the printed areas can be intercompared with the assumption that their optical structure is similar.

Al back surface fields (BSF) are used for most standard industrial Si solar cells today. A layer of Al is printed on the back side of the Si wafer and then fired to create a p+ Al-doped Si layer, which repels minority charge carriers in a p-type Si solar cell. The resulting back SRV is usually on the order of 200 - 600 cm/s [3,4].

* Corresponding author. Tel.: +47 63806021.
E-mail address: frode.klow@ife.no

Selection and peer-review under responsibility of Guy Beaucarne, Gunnar Schubert and Jaap Hoornstra
doi:10.1016/j.egypro.2013.11.084

In this work, QSSPC-calibrated PLI was used to determine the effective rear surface recombination velocity $S_{rear,eff}$ of p-type Si FZ wafers after processing of screen printed Al contacts with varying paste thickness and firing temperatures. $S_{rear,eff}$ is caused by the recombination at the back surface and the repulsion of minority carriers from this surface due to the field effect of the Al BSF. The uncertainties in the $S_{rear,eff}$ measurement are discussed. The paste thickness was varied by changing the screen printer snap off parameter, and the resulting BSF thickness was investigated by scanning electron microscopy.

2. Experimental details

2.1. Sample preparation

The samples were chemically polished (100)-oriented p-type Si FZ wafers of 1.1 Ωcm resistivity and 260 µm thick. The circular wafers were cut into four pieces by laser. The samples were weighed and measured to calculate area and thickness. An HF dip in 5 % HF in di-ionized water was done before PECVD passivation with SiNx. The deposition was done at 400 °C with a resulting refractive index of 2.05. One reference sample from each wafer was double side passivated, and the other samples were screen printed with commercially available Al paste.

Paste thickness was varied by changing the snap-off parameter of the screen printer. Changing the snap-off to vary the printing thickness is well known, but an often used alternative is to change the emulsion thickness [5,6]. Changing the snap-off has the advantage that it is a software parameter adjustment and therefore quicker, and it is easier to get different thicknesses. Fig. 1 shows the paste weight as a function of the snap-off for two different screens from an experiment to determine the effect of the snap-off parameter on the paste amount.

A potential problem with changing the snap-off is that the paste weight changes rapidly in a small snap-off interval, so it can be difficult to control. This also leads to an uncertainty in the paste thickness across the wafer as small changes in the screen, as well as varying squeegee pressure, have a larger effect. One should also be careful in changing the snap-off too much as this can reduce the screen lifetime by stretching the mesh.

Firing was done in a four zone belt furnace, using three different profiles, to give a full-area BSF. The peak set point temperatures were 885 °C, 930 °C and 970 °C, with a belt speed of 480 cm/min. The firing temperature of 930 °C is an optimized set point temperature for an industrial Si solar cell, so 885 °C and 970 °C can be seen as underfired and overfired, respectively. Cross sections of the samples were investigated by scanning electron microscopy (SEM). The samples were broken along the crystal edge and etched in 1:3:6-HF:HNO_3:CH_3COOH for 10 seconds to enhance the contrast between the more heavily doped p+ BSF layer and the lightly doped p-type Si substrate [7]. Layer thicknesses were found by tracing the borders of the BSF and eutectic regions, as seen in Fig. 2, and then calculating the distances betweeen the lines.

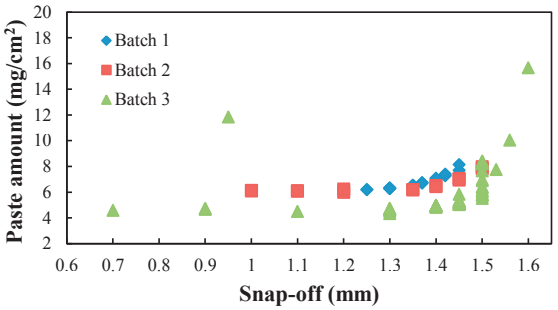

Fig. 1. The dependence of the printed paste amount on the snap off parameter. Paste weight per area measured after drying. Batch 1 and 2 were printed with a different emulsion than Batch 3. The measurement point at a snap off 0.95 mm for Batch 3 is taken as an outlier as it was the first wafer printed.

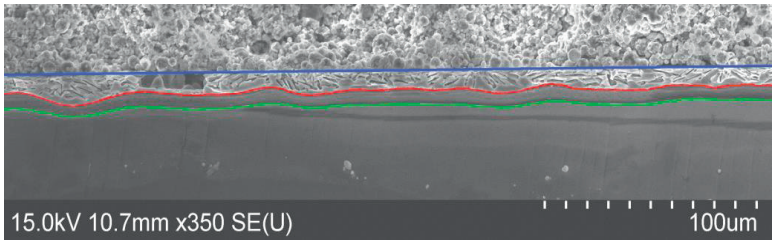

Fig. 2. SEM image of the BSF of sample W2-4, fired at 970 °C. The average BSF depth and uniformity were calculated based on sections about 350 µm long, consisting of more than 1000 points. The drawn lines indicate the edges of the eutectic layer (blue and red) and the BSF layer (red and green) , and were used as a basis for uncertainty measurements.

2.2. PLI lifetime measurements and SRV

PLI was used to measure the effective lifetime τ_{eff} of the samples, with an incident photon flux from the excitation laser of 2.97×10^{17} $cm^{-2}s^{-1}$, at a wavelength of 808 nm. Every point of the effective lifetime map $\tau_{eff;x,y}$ is calculated according to

$$\tau_{\mathrm{eff;x,y}} = \Delta n_{x,y} \frac{W}{\Phi(1-R_{front})}. \quad (1)$$

where the injection level $\Delta n_{x,y}$, is calculated based on the PL intensity measured, and the incident photon flux Φ is measured by a Si solar cell reference. R_{front} is the reflectivity of the sample at 808 nm, and W is the thickness of the sample.

As shown in Fig. 3, a reference sample was calibrated using QSSPC and the samples were imaged by PLI. The lifetime value chosen as representative was selected averaging the best area of each sample with a size equal to the QSSPC coil. This was done to minimize effects such as belt tracks and scratches. Four images were taken of each sample in different configurations.

The effective lifetime of the sample τ_{eff} is the sum of the bulk lifetime τ_b and surface lifetime τ_s contributions

$$\frac{1}{\tau_{\mathrm{eff}}} = \frac{1}{\tau_b} + \frac{1}{\tau_s}. \quad (2)$$

To calculate the effective back side SRV, $S_{rear,eff}$, for the metallized samples, the contribution from the front side SRV, S_{front}, is found for the reference samples using [8], assuming that S_{front} and $S_{rear,eff}$ for this sample are equal (S):

$$\tau_s = \frac{W}{2S} + \frac{1}{D}\left(\frac{W}{\pi}\right)^2, \quad (3)$$

which is a simplification of the general equation

$$\tan(\alpha_0 W) = (S_{front} + S_{rear,eff})/(\alpha_0 D - \frac{S_{front}S_{rear,eff}}{\alpha_0 D}), \quad \alpha_0 = \sqrt{(\frac{1}{\tau_s D})}, \quad (4)$$

for $S = S_{front} = S_{rear,eff}$. W is the sample thickness and D is the diffusion coefficient of the excess carriers. Eq. 4 can then be used to find $S_{rear,eff}$ for the metallized samples, with $S_{front,reference} = S_{front,metallized}$.

Another useful parameter is the BSF saturation current $J_{0,BSF}$. The total recombination current due to the BSF layer is

$$J_{rec,BSF} = J_{0,BSF}\left(e^{\frac{qV}{k_B T}} - 1\right), \quad (5)$$

with an applied voltage V. q is the elementary charge, k_B is the Boltzmann constant and T is the temperature. $J_{0,BSF}$ is related to $S_{rear,eff}$ through [9]

$$J_{0,BSF} = S_{rear,eff}\left(\frac{qn_i^2}{\Delta n + n_0 + p_0}\right), \quad (6)$$

assuming At 25 °C, the intrinsic carrier concentration n_i in Si is 8.30 x 10^9 cm^{-3} [10]. Δn is the injection level from Eq. 1 and n_0 and p_0 are the equilibrium electron and hole densities in the bulk ($p_0 \approx N_a = 1.3 \times 10^{16}$ $cm^{-3} \gg n_0$).

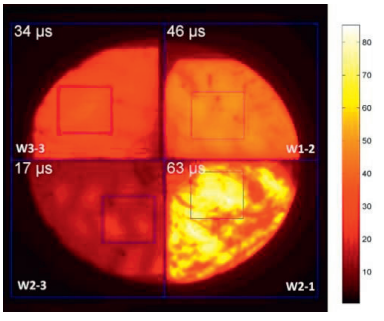

Fig. 3. Variation of lifetime for samples fired at different peak temperatures. W2-1 is the QSSPC calibrated reference sample. W2-3, W3-3 and W3-4 were fired at 885 °C, 930 °C and 970 °C, respectively.

3. Results and discussion

3.1. $S_{rear,eff}$ and BSF results

The $S_{rear,eff}$, calculated using Eq. 4, as a function of paste amount for three different firing temperatures is shown in Fig. 4, and the $S_{rear,eff}$ as a function of these temperatures is shown in Fig. 5. Fig. 4 also shows uncertainties that will be discussed in section 3.2. The $S_{rear,eff}$ improves when fired at increasingly higher temperatures. 975 °C is normally too hot for industrial Si solar cell processing, but this is because of shunting of the depletion region by the front contacts. On the back side of a solar cell, more Si can be incorporated into the melted Al at higher temperatures. When the melt cools, the Si is segregated out from the melt because the composition follows the liquidus curve of the Al-Si phase diagram. This Si crystallizes at the interface of the two layers and incorporates the solid solubility concentration of Al, creating the BSF layer. This effect can be approximated as [11,12]

$$d_{p+} = \frac{m_{Al}}{A\,\rho_{Si}} \left(\frac{L(T_{peak})}{100 - L(T_{peak})} - \frac{L(T_{eut})}{100 - L(T_{eut})} \right), \tag{7}$$

where m_{Al} is the Al weight, A is the printed area, and ρ_{Si} is the density of silicon. $L(T_{peak})$ and $L(T_{eut})$ are the percentages of Si in the Al melt at the peak temperature and the eutectic temperature, respectively, which can be read from the Al-Si phase diagram.

Eq. 7 can be solved using $L(T_{eut})$ equal to 12.2 % from the Al-Si phase diagram [13], a paste amount of 8 mg/cm^2, and assuming the peak firing set points of 885 °C, 930 °C and 975 °C corresponds to sample temperatures of 755 °C, 800 °C and 845 °C, respectively. This gives BSF thicknesses of about 6µm, 8.5 µm, and 11 µm, respectively, but this is lower than those measured. According to Eq. 7, the BSF thickness should also increase for higher paste amounts. However, in Fig. 4 the $S_{rear,eff}$ is best for a medium paste amount of 7.5 to 8.1 mg/cm^2. Krause et al. [12] and Huster [14] explain the deviations for real firing processes compared to Eq. 7.

- For a given set point firing temperature, the actual material temperature will be different depending on the masses of the samples, so a thicker paste will give a lower temperature at the BSF/Si interface
- There is a limit to the Si diffusion into the Al paste, so that not all the Al will take part in the process
- Not all the diffused Si will go back to the surface due to rapid cooling

These effects can all be used to explain the increase in $S_{rear,eff}$ for the largest paste amounts, and can also explain why the expected BSF thickness is higher than the measured thickness. It has also been found that a change in the temperature ramp up can affect the BSF thickness [15]. However, as shown in Fig. 6, the BSF thickness uncertainty is so large that a relationship between the paste amount and BSF thickness can not be firmly established. One possible reason for this is the uncertainty in the snap off variation during printing. An optimized firing profile for each paste amount could also help emphasize this relationship. The uncertainty is the standard deviation of the BSF thickness across an approximately 350 µm representative part of the sample, as shown in Fig. 2.

This uncertainty also gives a measure of the homogeneity of the BSF and eutectic layer thickness, and is graphed in Fig. 8 and Fig. 9. The absolute deviation of the BSF thickness increases for higher firing temperatures, but the opposite is true when using relative numbers. There is no such pattern for the eutectic thickness. A higher peak firing temperature

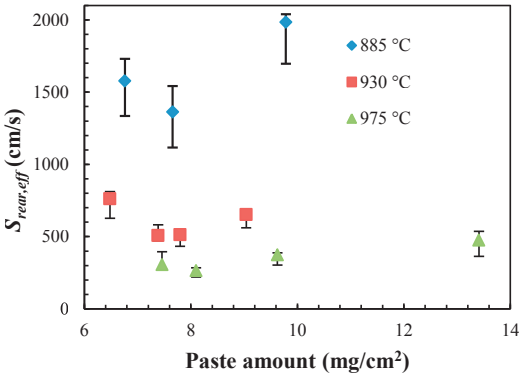

Fig.4. Back surface recombination velocity as a function of the amount of paste for different firing temperatures. Error bars show uncertainties based on minimum and maximum values from PLI across several images, and the uncertainty in the inital bulk lifetime of the wafers.

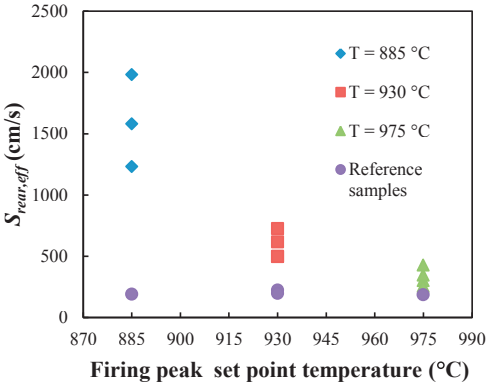

Fig. 5. $S_{rear,eff}$ and the firing temperature, including reference samples.

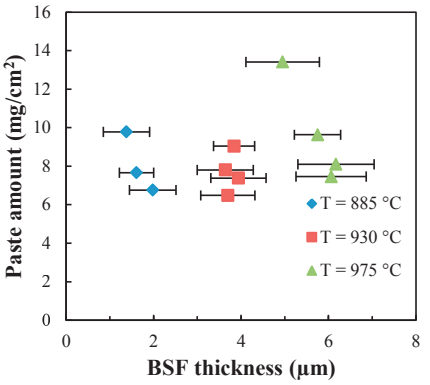

Fig. 6. BSF thickness variations as a result of varying paste amount. The uncertainty bars of the BSF thickness show the standard deviation of the measurement. This deviation was found by imaging a representative 350 µm part of the BSF.

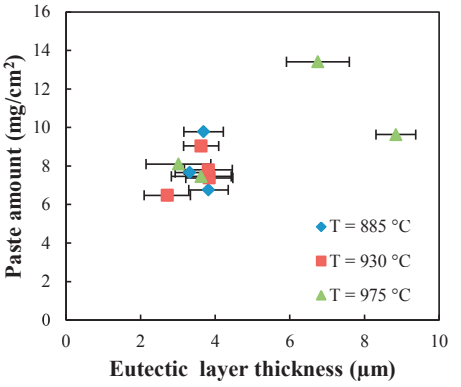

Fig.7. Eutectic thickness variations as a result of varying paste amount. Only for large paste amounts and a high firing temperature does the eutectic thickness increase.

should increase the temperature ramp up rate, which has been found to increase the eutectic layer uniformity [7][15]. However, the standard deviation is not a good measure in this case because it only takes into account the distribution of thicknesses and not the change in thicknesses. Visually from the SEM images it is clear that the eutectic thickness changes more for thin BSF thicknesses.

There does not seem to be a relationship between the BSF deviation and the eutectic deviation, which means that a change in the eutectic layer does not give a change in the BSF layer beneath. The reason for the non-uniformity of the eutectic layers is therefore solely attributed to the local melting of Al at the Al-Si interface during firing. An inhomogeneous eutectic layer is possibly a worse reflector than a smooth layer because the interface between the eutectic layer and the BSF layer is where the back side reflection occurs, and the inhomogeneous surface could make the reflection more diffuse. It can also increase the back surface recombination due to the larger surface.

A saturation of the BSF thickness was found for the thickest pastes at a firing temperature above 975 °C, as shown in Fig. 7. Krause et al. [12] found this effect to occur because the BSF formation process was limited by Si diffusion from the eutectic back to the Si-eutectic interface. Interestingly, the effect does not seem to occur for the other firing temperatures, even though the thickest paste used for those is comparable to one of the saturated samples at 975 °C. Neither is the saturation effect largest for the thickest paste sample. However, for this sample the paste peeled off during the firing process.

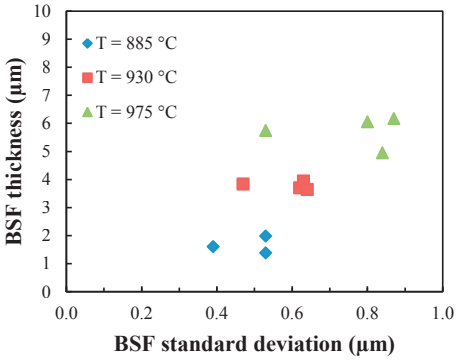

Fig. 8. The absolute BSF deviation from average increases with increasing BSF thickness. The BSF deviation as a percentage of the BSF thickness decreases, however. Areas of the cross section where there is no BSF layer are not counted towards the total deviation.

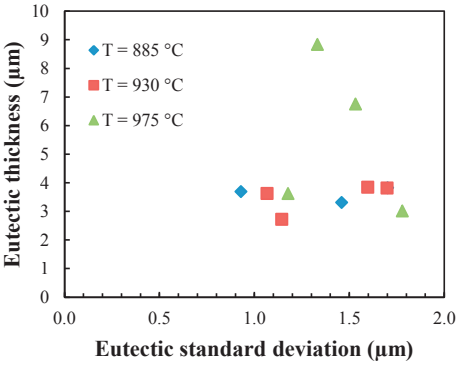

Fig. 9. The eutectic thickness varies between 2.7 and 3.9 µm and does not depend on the firing temperature. The two top points are the saturated BSF samples. Areas of the cross section where there is no eutectic layer are not counted towards the total deviation, because paste residuals occasionally cover this layer.

3.2. BSF saturation current $J_{0,BSF}$

The $S_{rear,eff}$ were converted into $J_{0,BSF}$ values as detailed in section 2.2, and are presented in Table 1. The $S_{rear,eff}$ are based on assumptions that will be discussed in the next section, and because these measurements have been done on metallized surfaces they are not comparable to other experimental results. Altermatt et al. [16] reports that typical $J_{0,BSF}$ values are between 600 fA/cm^2 and 900 fA/cm^2, however, a $J_{0,BSF}$ of 274 fA/cm^2 was extracted in [17]. In a modelling study by Rüdiger et al. [18], a defect free limit of 250-300 fA/cm^2 is shown for a BSF thickness of 6 µm, so it is obvious that the results presented in Table 1 are too low due to the metallization.

Table 1. $J_{0,BSF}$ based on an initial estimated $S_{rear,eff}$ calculated from the lower limit of the bulk lifetime, average PLI measured effective lifetime, reference sample belonging to wafer of sample, and no reflection from metallized surface. Sample names with a last digit of 1 are reference samples.

Sample	Firing temp. (°C)	Initial estimated $S_{rear,eff}$ (cm/s)	$J_{0,BSF}$ (fA/cm^2)
W2-1	885	172	137
W2-2	885	1983	1643
W2-3	885	1576	1303
W4-2	885	1362	1125
W1-1	930	220	177
W1-4	930	507	413
W3-1	930	171	136
W3-2	930	653	534
W3-3	930	762	625
W4-3	930	512	417
W1-2	975	306	247
W2-4	975	374	302
W3-4	975	476	387
W4-1	975	184	147
W4-4	975	264	212

3.3. PLI uncertainties

Because of the reliance of the PLI technique on homogenous optics within an image, there are uncertainties for a practical experiment where front side reflections and surface roughness might not be exactly the same for the sample as for the calibrated reference. Another uncertainty is that the detector picks up some signals that have been emitted at an angle, giving a more diffuse lifetime image. Even though the detector filters out most of the laser excitation light, superimposed laser light will create a small signal [19]. These uncertainties are measurement errors that were not dealt with in this work.

The increased signal due to metallized surfaces underestimates $S_{rear,eff}$, so the values estimated in this paper are consequently too low. By putting a reflecting surface under the reference samples, an estimated maximum $S_{rear,eff}$ can be attained. Slightly crumpled Al foil was put under the reference samples and giving an average effective lifetime increase of 39-49 %, and values up to 60 %. The effect on $S_{rear,eff}$ is even higher, with relative $S_{rear,eff}$ increases of 82 to 140 % estimated for an effective lifetime increase of 50 %. However, the Al foil is likely to exaggerate the reflection effect because an Al BSF gives more diffuse reflection.

The error bars of Fig. 4 are based on three uncertainties, which are shown in Table 3, and combined under the "Combined" column. These are uncertainties that are unrelated to reflection off metallization. The first uncertainty added is a PLI measurement uncertainty. Fig. 10 shows the PLI lifetime data for each image of each sample, superimposed for brevity, while the average effective lifetime and the standard deviation of the lifetimes measured for each sample is stated in the legend. While the averages are used for the main points of Fig. 4 and 5, there is a variation in the lifetime between the images, which limits the accuracy of the technique. The shorter lifetimes are more sensitive to changes, giving larger uncertainties for larger recombination rates.

When calculating the $S_{rear,eff}$ of metallized samples based on the assumptions presented in section 2.2, the front SRV of these samples is assumed to be the same as for the reference samples, but this is not necessarily true. Both reference and metallized samples can change during processing due to for example scratching. In this study, three reference samples fired

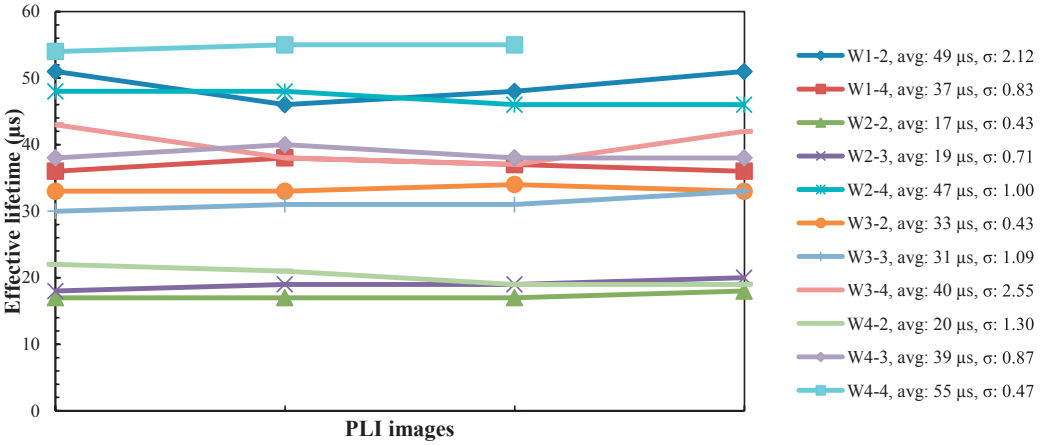

Fig. 10. The collected PLI data, not including reference samples. Several samples were imaged simultaneously for each measurement, but there is no correlation of this on the x-axis; the measurements are superimposed in this graph for clarity. The legend shows the average effective lifetime measured (avg) and the standard deviation (σ) for each sample.

at 885 °C, 930 °C and 975 °C had initial effective lifetimes of 72 µs, 73 µs and 69 µs, respectively. A fourth reference sample had a measured lifetime of only 59 µs. In this work, the reference used was the one belonging to the same wafer as the metallized samples. By comparing the difference of the lowest reference lifetime and the highest, an uncertainty can be found. Table 2 gives the percentage difference of the effective lifetimes of 59 and 73 µs, as well as a hypothetical difference between measured lifetimes 10 times as high, to show how the uncertainty decreases for excellent passivated samples.

An upper and a lower limit for the bulk lifetime of the reference samples are used to calculate the front SRV, using Eq. 2 and 3. The lower limit is the highest measured bulk lifetime for the wafers used with as good passivation as possible, and the upper limit is when the bulk lifetime is set to the intrinsic carrier lifetime at bulk doping level [20]. This difference in the front SRV is of about 4 % with the low lifetimes in this study, but can be significantly higher with higher lifetimes and should be taken into account.

Another uncertainty related to low front SRV is that the excited carriers with shorter lifetimes are more affected by the front recombination. The PLI excitation light is mostly absorbed near the top of the wafer. For low lifetime samples the excited charge carriers will not diffuse and distribute evenly across the wafer, and therefore be more affected by the front SRV than the back SRV. This uncertainty has not been added to Table 3 or Fig. 4.

Table 2. Uncertainties for different measured effective lifetimes used for calculations of $S_{rear,eff}$. 73 and 59 µs are based on the samples used in this work, while 730 and 590 µs are hypothetical to show how the uncertainty decreases with higher lifetimes. Calculations are done using the lower limit of the bulk lifetime.

Firing temperature (°C)	$S_{rear,eff}$ calculated for 73 µs reference effective lifetime (cm/s)	$S_{rear,eff}$ calculated for 59 µs reference effective lifetime (cm/s)	Percent difference (%)	$S_{rear,eff}$ calculated for 730 µs reference effective lifetime (cm/s)	$S_{rear,eff}$ calculated for 590 µs reference effective lifetime	Percent difference (%)
885	1985.1	1853.7	7.09	2583.1	2565.0	0.70
885	1577.6	1473.1	7.10	2040.1	2026.4	0.67
885	1387.7	1293.9	7.24	1797.3	1785.3	0.67
930	564.3	507.1	11.29	806.4	799.5	0.86
930	653.2	592.6	10.23	910.5	903.1	0.81
930	761.8	696.0	9.46	1044.6	1036.5	0.79
930	527.8	472.0	11.84	764.0	757.3	0.89
975	355.3	305.8	16.19	562.8	556.9	1.06
975	374.2	324.1	15.46	584.1	578.1	1.03
975	475.5	421.9	12.72	700.6	694.2	0.92
975	277.4	230.7	20.25	471.5	466.0	1.17

Table 3. $S_{rear,eff}$ uncertainties in percent based on an initial estimated $S_{rear,eff}$ calculated from the lower limit of the bulk lifetime, average PLI measured effective lifetime, reference sample belonging to wafer of sample, and no reflection from metallized surface. Sample names with a last digit of 1 are reference samples.

			Bulk lifetime uncertainty		PLI measurement effective lifetime		Reference sample deviations		Combined		Metallized surface reflection
Sample	Firing temp. (°C)	Initial estimated $S_{rear,eff}$ (cm/s)	Low (%)	High (%)	Low (%)	High (%)	Low (%)	High (%)	Low (%)	High (%)	50% effective lifetime increase (%)
W2-1	885	172	0	5	0	35	-25	0	-29	36	0
W2-2	885	1983	0	1	-7	3	-7	0	-14	3	140
W2-3	885	1576	0	1	-8	10	-7	0	-15	10	113
W4-2	885	1362	0	1	-13	11	-5	2	-18	13	104
W1-1	930	220	0	4	-13	24	0	21	-17	46	0
W1-4	930	507	0	2	-5	3	0	11	-7	15	88
W3-1	930	171	0	5	0	103	-25	0	-29	103	0
W3-2	930	653	0	1	-3	1	-9	0	-14	1	84
W3-3	930	762	0	1	-8	7	-9	0	-18	7	86
W4-3	930	512	0	2	-6	2	-8	3	-15	5	84
W1-2	975	306	0	3	-7	12	0	16	-10	29	95
W2-4	975	374	0	2	-3	4	-13	0	-19	4	84
W3-4	975	476	0	2	-11	13	-11	0	-24	13	82
W4-1	975	184	0	4	-20	24	-17	7	-40	31	0
W4-4	975	264	0	3	-1	2	-13	5	-17	7	92

4. Summary

PLI lifetime measurements were used to calculate the rear SRV of metallized samples, with variations of paste amount and firing temperatures. Paste amount was varied by changing the snap-off parameter of the screen printer. A discussion of uncertainties in the $S_{rear,eff}$ calculations was made with a focus on low lifetime samples, and the uncertainties were found to influence the calculated $S_{rear,eff}$. These uncertainties are not necessarily inherent with the PLI method, but care should be taken to reduce the front side recombination where possible.

BSF layers were investigated by SEM. BSF thicknesses between 1.4 and 6.2 µm were found, and the higher temperatures resulted in thicker BSF layers and better SRVs. A standard deviation of the BSF uniformity was found, and was useful in dismissing correlations between paste amount and BSF thickness. The eutectic layer is found to be of a very consistent thickness across all samples, except for the two samples with the thickest paste fired at the highest temperature, which have a saturated BSF layer and a thicker eutectic layer.

References

[1] Trupke T, Bardos RA, Abbott MD. Self-consistent calibration of photoluminescence and photoconductance lifetime measurements. Applied Physics Letters, vol. 87, no. 18, p. 184102, 2005.
[2] Trupke T, Bardos RA, Schubert MC, Warta W. Photoluminescence imaging of silicon wafers. Applied Physics Letters, 89(4), 044107-044107, 2006.
[3] Narasinha S, Rohatgi A. Optimized aluminum back surface field techniques for silicon solar cells. 26th IEEE Photovoltaic Specialists Conference, pp. 63–66, 1997.
[4] Peters S. Rapid thermal processing of crystalline silicon materials and solar cells. UFO Atelier für Gestaltung und Verlag, 2004.
[5] Salami J, Cruz B, Shaikh A. Paste Development for Low Cost High Efficiency. 16th Workshop on Crystalline Silicon Solar Cells & Modules: Materials and Processes, Denver, Colorado, 2006.
[6] Khadilkar C, Kim S, Shaikh A, Sridharan S, Pham T. Characterization of Al Back Contact in a Silicon Solar Cell. Presented at the International PVSEC-15, Shanghai, China, 2005.
[7] Meemongkolkiat V, Hilali M, Rohatgi A. Investigation of RTP and belt fired screen printed Al-BSF on textured and planar back surfaces of silicon solar cells. Photovoltaic Energy Conversion, 2003. Proceedings of 3rd World Conference on. Vol. 2. IEEE, 2003.
[8] Sproul AB. Dimensionless solution of the equation describing the effect of surface recombination of carrier decay in semiconductors. J. Appl. Phys. 76, 2851–2854, 1994.

[9] Fischer, B. Loss analysis of crystalline silicon solar cells using photoconductance and quantum efficiency measurements. Cuvillier, 2003.
[10] Misiakos K, Tsamakis D. Accurate measurements of the silicon intrinsic carrier density from 78 to 340 K. Journal of applied physics 74.5: 3293-3297, 1993.
[11] del Alamo J, Eguren J, Luque A. Operating limits of Al-alloyed high-low junctions for BSF solar cells. Solid-State Electronics 24, 415–420, 1981.
[12] Krause J, Woehl R, Rauer M, Schmiga C, Wilde J, Biro D. Microstructural and electrical properties of different-sized aluminum-alloyed contacts and their layer system on silicon surfaces. Solar Energy Materials and Solar Cells 95.8: 2151-2160, 2011.
[13] Udovskii AL, Karpushkin VN, Kozodaeva EA, Calphad 19, 245–277, 1995.
[14] Huster F. Investigation of the alloying process of screen printed aluminium pastes for the BSF formation on silicon solar cells. Proceedings of the 20th European Photovoltaic Solar Energy Conference, 2005.
[15] Park S, Bae S, Kim H, Kim S, Do Kim Y, Park H, Kim S, Tark SJ, Son CS, Kim D. Effects of controllable process factors on Al rear surface bumps in Si solar cells. Current Applied Physics, vol. 12, no. 1, pp. 17–22, 2012.
[16] Altermatt PP, Steingrube S, Yang Y, Sprodowski C, Dezhdar T, Koc S, Veith B et al. Highly predictive modelling of entire Si solar cells for industrial applications. In Proc. 24th Eur. Photovoltaic Solar Energy Conf, pp. 901-906. 2009.
[17] Fellmeth T, Mack S, Bartsch J, Erath D, Jager U, Preu R, Clement F, Biro D. 20.1% efficient silicon solar cell with aluminum back surface field. Electron Device Letters, IEEE, 32(8), 1101-1103. 2011.
[18] Rüdiger M, Rauer M, Schmiga C, Hermle M. Effect of incomplete ionization for the description of highly aluminum-doped silicon. Journal of applied physics, 110, 024508. 2011.
[19] Giesecke JA, The M, Kasemann M, Warta W. Spatially Resolved Characterization of Silicon As-Cut Wafers with Photoluminescence Imaging. Progress in Photovoltaics: Research and Applications 17.4: 217-225, 2009.
[20] Aberle AG. Chapter 2 in Crystalline silicon solar cells: advanced surface passivation and analysis. Centre for Photovoltaic Engineering. University of New South Wales, 1999.